


Article

Study on the Convective Heat Transfer and Fluid Flow of Mini-Channel with High Aspect Ratio of Neutron Production Target

Peng Sun ^{1,2,3}, Yiping Lu ^{1,*}, Jianfei Tong ^{2,3,4,*}, Youlian Lu ^{2,3} , Tianjiao Liang ^{2,3} and Lingbo Zhu ^{1,2,3}

¹ School of Mechanical Power Engineering, Harbin University of Science and Technology, Harbin 150080, China; sunpeng@ihep.ac.cn (P.S.); zhulingbo@ihep.ac.cn (L.Z.)

² Institute of High Energy Physics, Chinese Academy of Sciences (CAS), Beijing 100049, China; luyi@ihep.ac.cn (Y.L.); tjliang@ihep.ac.cn (T.L.)

³ Spallation Neutron Source Science Center, Dongguan 523803, China

⁴ School of Energy Science and Engineering, Harbin Institute of Technology, Harbin 150001, China

* Correspondence: luyiping@hrbust.edu.cn (Y.L.); tongjf@ihep.ac.cn (J.T.)

Abstract: In order to provide a theoretical basis for the thermal design of the neutron production target, flow and heat transfer characteristics are studied by using numerical simulations and experiments. A rectangular mini-channel experimental model consistent with the geometric shape of the heat dissipation structure of neutron production target was established, in which the aspect ratio and gap thickness of the test channel were 53.8:1 and 1.3 mm, respectively. The experimental results indicate that the critical Re of the mini-channel is between 3500 and 4000, and when Re reaches 21,000, Nu can reach 160. The simulation results are in good agreement with the experimental data, and the numerical simulation method can be used for the variable structure optimization design of the target in the later stage. The relationship between the flow pressure drop of the target mini-channel and the aspect ratio and Re is obtained by numerical simulation. The maximum deviation between the correlation and the experimental value is 6%.

Keywords: rectangular channel; parallel plates; mini-channel; single-phase heat transfer; turbulent flow; critical Reynolds number; entrance region; spallation target



Citation: Sun, P.; Lu, Y.; Tong, J.; Lu, Y.; Liang, T.; Zhu, L. Study on the Convective Heat Transfer and Fluid Flow of Mini-Channel with High Aspect Ratio of Neutron Production Target. *Energies* **2021**, *14*, 4020. <https://doi.org/10.3390/en14134020>

Academic Editors: Simone Salvadori, Daniela Anna Misul, Mauro Carnevale and Fabrizio Ascione

Received: 11 May 2021
Accepted: 28 June 2021
Published: 3 July 2021

Publisher's Note: MDPI stays neutral with regard to jurisdictional claims in published maps and institutional affiliations.



Copyright: © 2021 by the authors. Licensee MDPI, Basel, Switzerland. This article is an open access article distributed under the terms and conditions of the Creative Commons Attribution (CC BY) license (<https://creativecommons.org/licenses/by/4.0/>).

1. Introduction

At present, the neutron production targets used by ISIS Neutron and Muon Source (ISIS) [1] and Chinese Spallation Neutron Source (CSNS) are compact solid tungsten targets (Figure 1a,b), which has higher safety than Spallation Neutron Source (SNS) [2], with liquid mercury target (Figure 1c) and lower volume ratio of cooling medium than Paul Scherrer Institute (PSI) [3], with an array of lead rods (Figure 1d). Compact solid tungsten targets with higher neutron generation efficiency have been more widely applied such as the newly built European Spallation Source (beam power up to 5 MW) and CSNS Phase II Project (beam power up to 500 kW). More than 50% of the proton power is deposited in the target, which will reduce structural strength and service life. Thus, it is very important to carefully design the target to reduce the temperature; a common method is to separate the solid tungsten target into multi-sliced targets and reduce the temperature by independent cooling.

In order to balance the neutron generation efficiency of the target and the heat flux of the target, the design height of the CSNS target is 70 mm, and to improve the volume ratio of the target material, the thickness of the cooling channel of the target is limited to 1–2 mm, forming a rectangular mini-channel with large aspect ratio, as shown in Figure 1b. It is already known that the target is easily damaged under high irradiation and high temperature, and therefore, to avoid the corrosion of the target surface caused by boiling heat transfer, it is necessary to limit the flow of cooling fluid in a single phase. Carrying

out theoretical and experimental research on the fluid flow and heat transfer of a single-sliced target under the condition of limited temperature, especially in the large aspect ratio mini-channel, is an important issue for target safety.

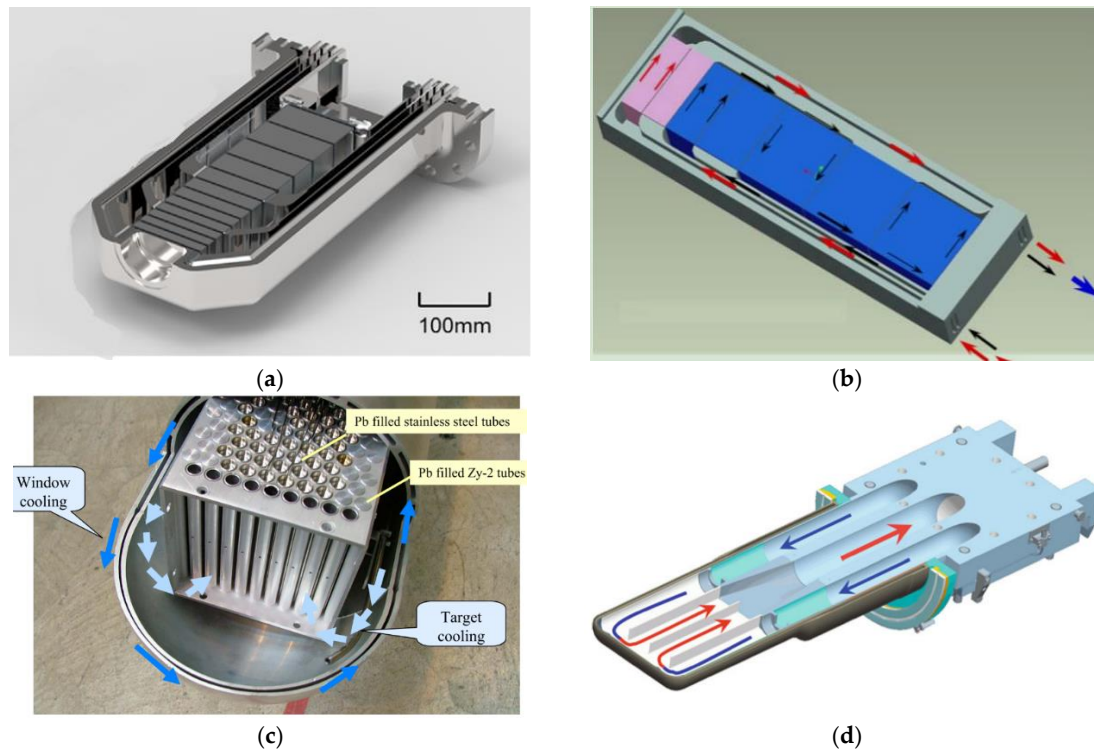


Figure 1. Different types of Spallation Neutron Target: (a) Spallation Neutron Target of ISIS; (b) Spallation Neutron Target of CSNS; (c) Spallation Neutron Target of PSI; (d) Spallation Neutron Target of SNS.

The flow past a sliced target is regarded as the mini-channel problem. The mini-channel cooling technique has some advantages, such as high convective coefficient, less coolant volume, and comparatively smaller cooling system size. It was first proposed by Tuckerman and Pease in 1981 [4], and it has been shown that micro/mini-channel cooling has gained much attention for its promising capability to remove high heat flux [5–7]. A significant amount of research has been dedicated to micro-channel transport on four aspects: (1) simple geometry of channels [8], (2) properties of coolants [9–11], (3) optimization of geometries [12,13], and (4) some research methods conducted by experimental research, numerical simulation, and empirical formula.

Forrest [14] experimentally studied the single-phase heat transfer in a narrow rectangular mini-channel heated on one side, with a gap thickness of the test channel of 1.96 mm. It concluded that the critical Re of the small channel test section is higher than that circular tube, and the correlation method of the circular tube cannot accurately estimate the single-phase heat transfer in the turbulent region. Wei [15] studied the influence of the aspect ratio and equivalent diameter of the channel on heat transfer through experiments and numerical simulations and verified that a smaller hydraulic diameter of the channel will lead to a larger aspect ratio and better heat transfer characteristics of the heat sink. They also explored the influence of boundary layer interruption on enhanced heat transfer. Muhammad [16] analyzed the effect of small channel geometry and inlet velocity on pressure drop, discovering that the flow resistance depends on the channel height, width, channel length, and coolant velocity. The influence of width is much greater than that of height. Ahmadi [17] optimized the cylindrical mini-channel with AL_2O_3 nanofluid as the cooling medium, and the results show that the cylinder diameter is the main factor affecting the heat transfer performance of the pipeline. Hassan [18] studied

the friction and thermal irreversibility of working fluids in microchannel heat transfer. The advantages and disadvantages of nanofluids compared with water in microchannel heat transfer were evaluated by entropy generation. Zheng [19] used the CFD method to study the heat transfer characteristics in the cone–column combined radiator of electronic components and analyzed the enhanced heat transfer effect of force mini-channel. Woodward [20] used graphite material to produce a cooling mini-channel for battery cooling, and a large number of experiments show that the new microchannel can reduce the peak measured temperature and the surface temperature gradient by 8 °C and 5 °C, respectively. In [21], the cyclotron resonator was cooled by mini-channels, and measured pressure drop data were used to validate the corresponding numerical CFD models, developed with the commercial software STAR-CCM+. Li et al. [22] analyzed the condensation flow and heat transfer performance in printed circuit heat exchanger (PCHE) mini-channels by using experiments and numerical simulation and discussed the influence of pressure and mass flow on friction resistance.

Although there are many studies on heat transfer in mini-channels, few experimental studies exist on targets with large aspect ratios under high heat flux. Therefore, the flow and heat transfer of sliced targets with large aspect ratios are studied through experimental research and numerical simulation, which provides theoretical guidance for target design and reduces the development cycle to improve the reliability of target design. This is the main motivation behind this study. It is worth noting that the present work aims at three major issues: (1) how Re affects heat transfer coefficients and resistance coefficients at mini-channels with high aspect ratio and whether the heat transfer coefficients can be calculated by using the classical empirical formula of the circular tube; (2) what is the range of critical Reynolds number for flow in mini-channels with high aspect ratio; (3) how the aspect ratio affects flow resistance in the water-cooled mini-channels of the neutron production targets.

2. Experimental Analysis

2.1. Experimental Setup

A thermal–hydraulic test loop was constructed to accommodate a high aspect ratio of a rectangular channel to simulate the coolant channel of the first target in the spallation target. A mini-channel heat sink with a height of 70 mm and a length of 170 mm was designed for providing the constant heat flux on the wall adjacent to the coolant. The aspect ratio and gap thickness of the test channel were 53.8:1 and 1.3 mm, respectively. As shown in Figure 2, the heat exchange channel was sealed by a glass cover plate and oxygen-free copper heater surface, which was made of 304 series stainless steel and hard sealing rubber ring. The heat exchange area on the surface of the mini-channel was 70 mm × 170 mm. The heater was made of oxygen-free copper, and 28 heating rods were packed inside. Each heating rod can provide a maximum power of 500 W, and the wall heat flux can reach the requirement of 0.9 MW/m² for the mini-channel heat sink. The heater and test section were modeled using ANSYS Fluent 17.0 software to ensure a constant wall heat flux in order to predict the maximum temperature and thermal gradient. Fabrication tolerances were used to account for the anticipated thermal expansion of components at operating temperatures. Transition sections were cut using wire electrical discharge machining to form a smooth inlet and exit to the channel to reduce vortex shedding and the required hydrodynamic development length. In this paper, the surface roughness of the channel was carefully controlled to be smaller, compared to the thickness of the viscous sublayer to ignore the influence of the roughness, which is already shown in [23]. The 20 thermometers were divided into 4 groups, which included up–front, down–front, up–back, and up–down. Each group was distributed along the flow direction. The distance between front and back rows was 4 mm, and upgroup and down-group thermometers were symmetrically distributed. The thermocouples were inserted into the heater box at 5 mm depth, as shown in Figure 3.



Figure 2. Scheme of rectangular coolant channel.

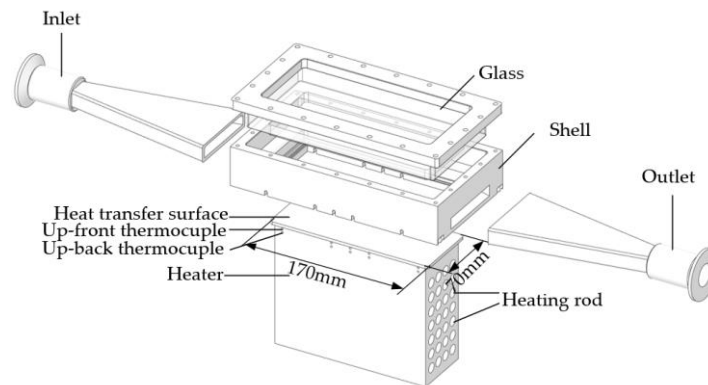


Figure 3. Explosive view of the rectangular coolant channel test section.

Figure 4 presents the experimental system, which simulates the operation of the channel heat sink. The deionized water is stored in the water tank as coolant and flows into the test section after regulating the flow through the pressure pump and valve. A vortex meter was used for flow measurement, and a four-wire platinum resistance temperature sensor (RTDS) was used to measure the inlet and outlet temperature of the test section; a differential pressure transducer was also installed at the inlet and outlet of the test section to permit accurate measurement of friction pressure drop during testing. The outdoor heat exchanger ensured the constant water temperature during the experiment. The water and surface were degassed prior to taking measurements. At each mass flux, when the temperature fluctuation of the thermocouple within 1 min is less than $1\text{ }^{\circ}\text{C}$, the heat transfer of the system could be considered to reach a steady state, with data collected through an Agilent 34,972 A Multifunction measurement unit.

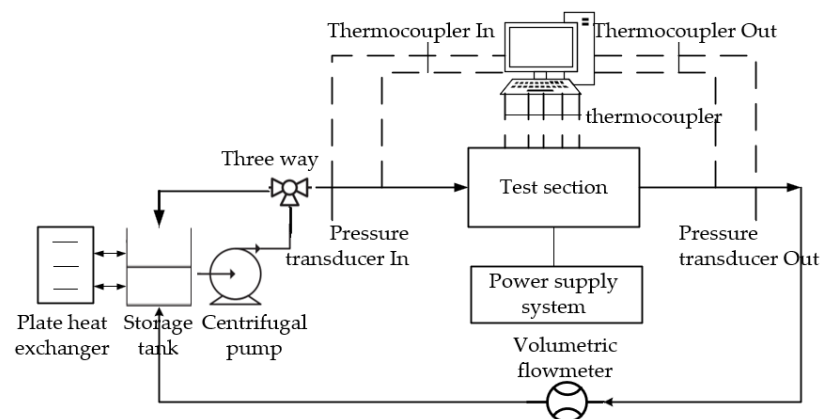


Figure 4. Schematic of the thermal–hydraulic test facility.

2.2. Data Acquisition

A number of parameters were used in this study, and a clear definition related to the geometry and flow under investigation is provided here [24]. Hydraulic diameter D_{hyd} is an important parameter to deal with the flow in noncircular pipes, which can be used to describe fluid mechanics and heat transfer.

$$D_{\text{hyd}} = \frac{4S}{P} \quad (1)$$

The channel area S and wet perimeter P are obtained from the width W and height H of the channel. The heating power Q was determined from the water temperature rise in the test section.

$$Q = q_v \rho C_p (T_f' - T_f'') \quad (2)$$

where T_f' , T_f'' are the inlet and outlet temperature measured by the thermometers, C_p is the specific heat capacity of the working medium, ρ is the density of the fluid, and q_v is the volume flow measured by the flowmeter. Heat transfer coefficient (h) can be estimated by Newton's cooling law Equation (3) as follows:

$$h_{\text{con}} = \frac{Q}{A_{\text{con}}(\bar{T}_w - T_f)} = \frac{Q}{HL(\bar{T}_w - T_f)} \quad (3)$$

where A_{con} is heat exchange area, L and H are the length and height of the heating surface, T_f is the average temperature of the working medium, obtained by the average temperature of inlet and outlet, and the average temperature of the heat exchange surface \bar{T}_w is obtained by the thermocouple.

$$\bar{T}_w = \bar{T}_{w2} + x_2 \times \left(\frac{\bar{T}_{w2} - \bar{T}_{w1}}{x_1} \right) \quad (4)$$

where \bar{T}_{w2} and \bar{T}_{w1} are the average temperature of the heater of front and back thermometers, respectively, obtained from the average value of five thermocouples in each row. x_2 is the distance between the first row thermocouples and the heat transfer wall, and x_1 is the distance between the first-row and the second-row thermocouples. The definition of Nusselt number is shown in Equation (5) as follows:

$$Nu = \frac{h_{\text{con}} D_{\text{hyd}}}{k} \quad (5)$$

where k is the thermal conductivity of the fluid at the average temperature. For simplification, the definition of Re can be written as in Equation (6).

$$Re = \frac{\rho \bar{u} D_h}{\mu}; \bar{u} = \frac{Q}{S} = \frac{q_v}{WH} \quad (6)$$

where \bar{u} is the average axial velocity of the fluid, S is the cross-sectional area of the channel, and μ is the dynamic viscosity of the fluid. The resistance coefficient is defined as Equation (7).

$$f = \frac{2\Delta P D_{\text{hyd}}}{\rho \bar{u}^2 L} \quad (7)$$

where ΔP is the pressure drop between the inlet and outlet of the experimental section, which is obtained by the experimental pressure difference meter.

2.3. Experimental Uncertainty Analysis

In order to evaluate the reliability of the measurement results, the uncertainty of the experiment was calculated according to Schultz and Col's theory [25] and Equation (8).

$$U_R = \left[\sum_{i=1}^n \left(\frac{\partial R}{\partial V_i} U_{V_i} \right)^2 \right]^{\frac{1}{2}} \quad (8)$$

where U_{V_i} is the absolute uncertainty of independent parameters, n is the total parameter, and V_i is an independent parameter.

The thermometer used in the experiment is calibrated by the constant temperature water tank, and the measurement error is less than 0.5 °C. The flowmeter and the pressure difference meter are instruments with an accuracy of 0.5. The relative error is less than 0.8% of the maximum range, and the error of the channel production process is less than 0.06 mm. The uncertainty of the Nu in the experiment is calculated as follows:

$$U_{D_{\text{hyd}}} = \sqrt{\left(\frac{2H}{W+H}U_W + \frac{-1}{(W+H)^2}2WHU_W\right)^2 + \left(\frac{2W}{W+H}U_H + \frac{-1}{(W+H)^2}2WHU_H\right)^2} \quad (9)$$

$$\frac{U_{D_{\text{hyd}}}}{D_{\text{hyd}}} = \sqrt{\frac{U_W^2}{W^2} - \frac{2U_W^2}{W(W+H)} + \frac{U_W^2}{(W+H)^2} + \frac{U_H^2}{H^2} - \frac{2U_H^2}{W(W+H)} + \frac{U_H^2}{(W+H)^2}} \quad (10)$$

$$U_{Nu} = \sqrt{\left(\frac{D_{\text{hyd}}}{\Delta T \cdot A_{\text{con}} \cdot k}U_{P_w}\right)^2 + \left(\frac{Q}{\Delta T \cdot A_{\text{con}} \cdot k}U_{D_{\text{hyd}}}\right)^2 + \left(-\frac{Q \cdot D_{\text{hyd}}}{\Delta T^2 \cdot A_{\text{con}} \cdot k}U_{\Delta T}\right)^2 + \left(-\frac{Q \cdot D_{\text{hyd}}}{A_{\text{con}}^2 \cdot \Delta T \cdot k}U_{A_{\text{con}}}\right)^2 + \left(-\frac{Q \cdot D_{\text{hyd}}}{k^2 \cdot A_{\text{con}} \cdot \Delta T}U_k\right)^2} \quad (11)$$

$$\frac{U_{Nu}}{Nu} = \sqrt{\left(\frac{U_Q}{Q}\right)^2 + \left(\frac{U_{D_{\text{hyd}}}}{D_{\text{hyd}}}\right)^2 + \left(-\frac{U_{\Delta T}}{\Delta T}\right)^2 + \left(-\frac{U_{A_{\text{con}}}}{A_{\text{con}}}\right)^2 + \left(-\frac{U_k}{k}\right)^2} \quad (12)$$

The relative uncertainty ratio of flow meter, channel length, the distance between two rows of thermocouple, the distance between the thermocouple and the heating surface are 2.5%, 1.2%, 0.5%, and 0.5%, respectively. T is the temperature of each thermocouple on the heater. The relative uncertainty of heat transfer coefficient Nu is better than 6%. The relative uncertainty of the friction coefficient is calculated as follows:

$$\frac{U_{\bar{u}}}{\bar{u}} = \sqrt{\frac{\left(\frac{1}{5}U_{q_v}\right)^2 + \left(-\frac{q_v}{S^2}U_S\right)^2}{(q_v/S)^2}} = \sqrt{\left(\frac{1}{q_v}U_Q\right)^2 + \left(-\frac{1}{S}U_S\right)^2} \quad (13)$$

$$\frac{U_f}{f} = \sqrt{\left(\frac{U_{\Delta P}}{\Delta P}\right)^2 + \left(\frac{U_{D_{\text{hyd}}}}{D_{\text{hyd}}}\right)^2 + \left(\frac{U_L}{L}\right)^2 + \left(\frac{U_{\bar{u}}}{\bar{u}}\right)^2 + \left(\frac{U_\rho}{\rho}\right)^2} \quad (14)$$

According to the equation and the uncertainty of the instrument, the relative error of $\frac{U_{\bar{u}}}{\bar{u}}$ is 4.8%. The relative uncertainty of the pressure difference meter is less than 0.7%, which results in the resistance coefficient f being better than 8%.

3. Numerical Analysis

3.1. Solution Domains and Boundary Conditions

In order to accurately simulate the experimental process, a corresponding model was established using Solidworks 2014 software according to the size of the test section, and the solution domain grid performed by meshing module in ANSYS Fluent is shown in Figure 5.

Physical properties of cooling water are shown in Table 1 and applied with the user function. The inlet temperature of the coolant was 28 °C, and the corresponding inlet velocity was set according to the Re . The outlet was set as the pressure outlet of the surface pressure of 0 Pa, and a heat source was applied to the surface of the heating rod.

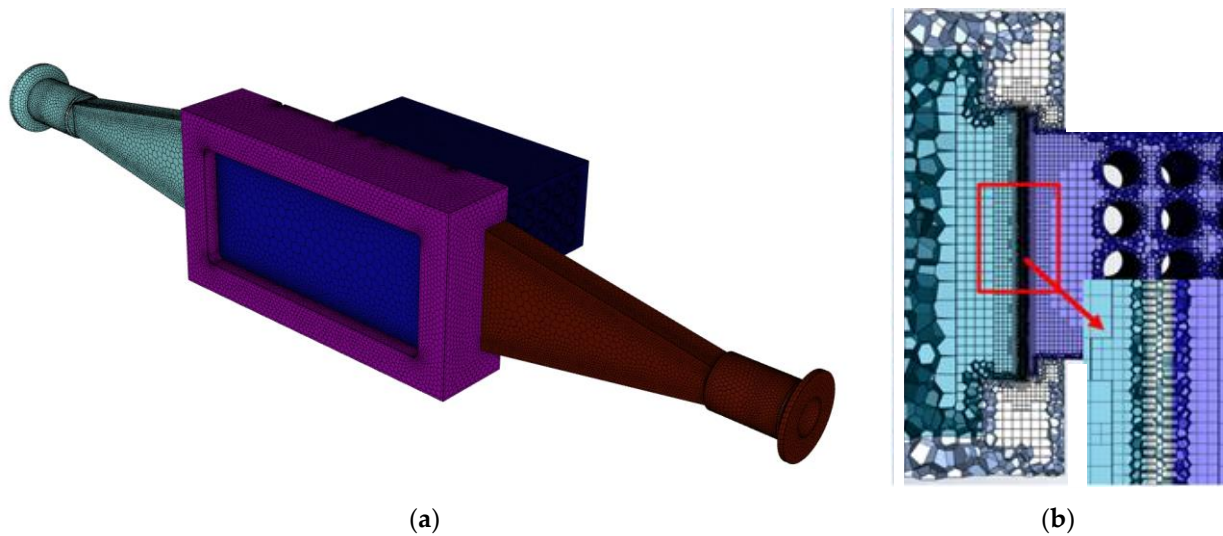


Figure 5. Mesh used in the numerical simulations: (a) integrate grid for experimental equipment; (b) local fluid grid.

Table 1. Physical properties of cooling water.

Physical Properties	Expression Function
ρ	$584.19017 + 3.5952 \times T - 0.00927 \times T^2 + 0.00000621362 \times T^3$
C_p	$1.03 \times 10^4 - 5.5 \times 10^1 \times T + 1.6 \times 10^{-1} \times T^2 - 1.64 \times 10^{-4} \times T^3 (T < 416 \text{ K})$ $5.47 \times 10^3 - 7.95 \times T + 1.23 \times 10^{-2} \times T^2 (T > 416 \text{ K})$
ν	$0.10741 - 9.3 \times 10^{-4} \times T + 2.7 \times 10^{-6} \times T^2 - 2.6 \times 10^{-9} \times T^3 (T < 416 \text{ K})$ $0.01686 - 1.1 \times 10^{-4} \times T + 2.73 \times 10^{-7} \times T^2 - 2.17 \times 10^{-10} \times T^3 (T > 416 \text{ K})$
k	$-1.71045 + 1.613 \times 10^{-2} \times T - 3.58 \times 10^{-5} \times T^2 + 2.61 \times 10^{-8} \times T^3$

3.2. Governing Equations

The numerical simulations were performed to obtain the flow and the temperature fields for steady-state operating conditions by the CFD method. The mass, momentum, and energy conservation equations calculated in this study are as follows:

$$\nabla \cdot u = 0 \quad (15)$$

$$u \cdot \nabla u = -\frac{1}{\rho} \nabla P + \frac{\mu}{\rho} \nabla^2 u \quad (16)$$

$$u \cdot \nabla T = \frac{k}{\rho C_p} \nabla^2 T \quad (17)$$

where u is the velocity vector, C_p is the fluid specific heat capacity, ρ is the fluid density, P is fluid pressure, k is fluid thermal conductivity. In steady-state flow, the time term can be ignored in the equation. A Two-equation K-omega SST model is used to solve the turbulent flow; the simulation equation is shown in Equation (18). Turbulent kinetic energy k and specific dissipation rate ω are obtained from the following transport equations:

$$\begin{aligned} \frac{\partial}{\partial t}(\rho k) + \frac{\partial}{\partial x_i}(\rho k u_i) &= \frac{\partial}{\partial x_j} \left(\Gamma_k \frac{\partial k}{\partial x_j} \right) + G_k - Y_k + S_k \\ \frac{\partial}{\partial t}(\rho \omega) + \frac{\partial}{\partial x_i}(\rho \omega u_i) &= \frac{\partial}{\partial x_j} \left(\Gamma_\omega \frac{\partial \omega}{\partial x_j} \right) + G_\omega - Y_\omega + S_\omega \end{aligned} \quad (18)$$

where G_k is the turbulent kinetic energy generated by the average velocity gradient, G_ω is the generation rate of ω , Γ_ω and Γ_k , Y_k and Y_ω is the effective diffusion coefficient and

turbulent dissipation of ω and k , respectively. S_k and S_ω are custom source terms. The effective diffusion coefficient is obtained by the following equation:

$$\begin{aligned}\Gamma_k &= \mu + \frac{\mu_t}{\sigma_k} \\ \Gamma_\omega &= \mu + \frac{\mu_t}{\sigma_\omega}\end{aligned}\quad (19)$$

where σ_k and σ_ω are the turbulent Prandtl number of k and ω respectively. The turbulent viscosity μ_t is obtained by the following equation:

$$\mu_t = \alpha^* \frac{\rho k}{\omega} \quad (20)$$

where α^* is the turbulent viscosity coefficient.

3.3. Solution and Grid Independence

A pressure-based solver was used to solve the momentum, mass, and energy equations, and the SIMPLEC algorithm was used for pressure–velocity coupling with the second-order upwind as the discretization scheme for the momentum, turbulent kinetic energy, and the turbulent dissipation rate. The absolute convergence criterion was set to be 10^{-6} for continuity equations, x–y–z velocities, k , ω , and 10^{-9} for the energy residual.

In order to accurately describe the turbulence and meet the requirements of $y^+ = 1$ and the grid growth rate of 1.2, the polyhexcore grids on both sides of the near-wall of the small channel were refined. Four groups of grids with different numbers were designed to verify the independence. As shown in Figure 6, the inlet pressure is taken as the monitoring parameter. The grid convergence index (GCI) was used to quantify the grid independence [26]. The fine-to-intermediate grid form (GCI_{43}) was 2.3%, while the intermediate-to-coarse grid form (GCI_{32}) was 3.5%. The value of $GCI_{32}/(r^p GCI_{43})$ was 0.96, which was approximately 1, indicating that the solutions were well within the asymptotic range of convergence.

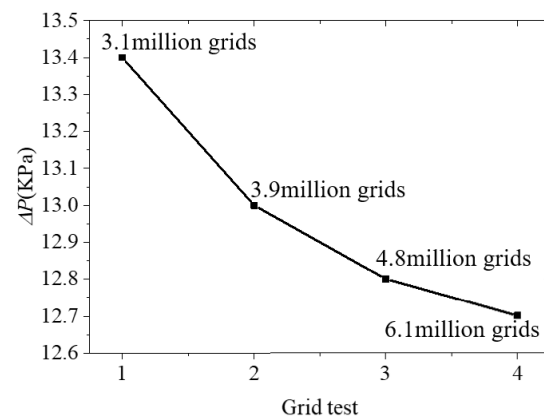


Figure 6. Grid independence test for the fluid region with pressure drop. Case parameters: $Re = 10,000$.

4. Results and Discussion

4.1. Analysis of Heat Transfer Characteristics

The governing Equations (15)–(20) were solved for turbulent flow at the corresponding boundary conditions. The values of temperature from four groups of thermocouples along the flow direction are shown in Figure 7a; the heat flux is 0.9 MW/m^2 , and Re is 15,000. Figure 7b–d is the numerical simulation results under this condition. The error bars are standard deviations of the repeated results of each thermocouple taken every five minutes in an hour at a steady state. It is shown that there is little difference between symmetrical measuring points along height direction, indicating the reliability of the measurement results and the uniformity of heat distribution along the height. The temperature distribution shows a trend of high in the middle and low at both ends, which

is related to the heat conduction at both ends of the flow inlet and the experimental body. The relationship between the average wall temperature and the flow rate obtained from the original data of the experimental measurement points and the formula is shown in Figure 8. The increase of the flow rate leads to the enhancement of the heat transfer capacity. The temperature of the heat exchange surface is close to the saturation temperature (120 °C) at the inlet mass flow rate of 6 Kg/min.

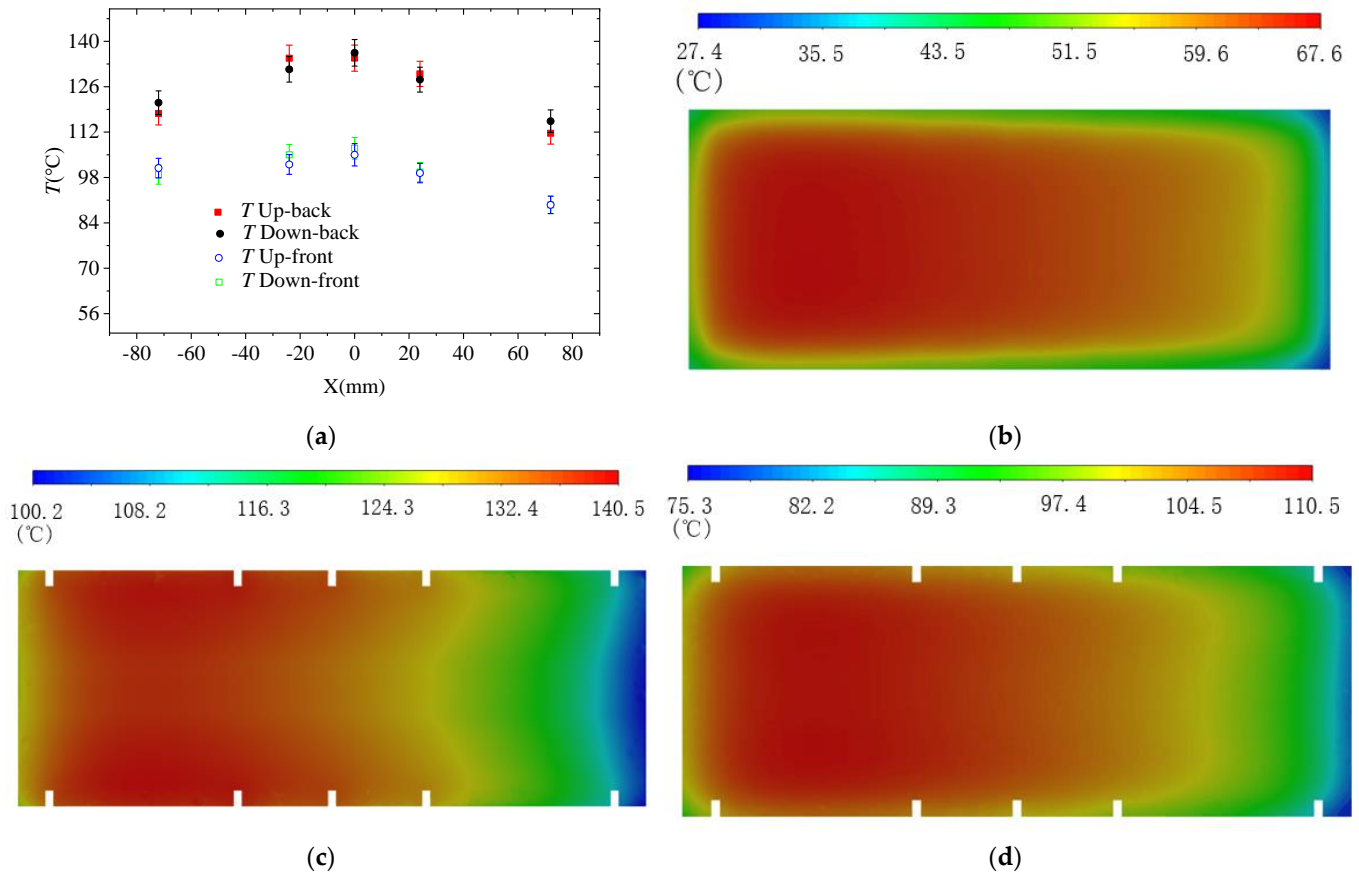


Figure 7. Temperature distribution: (a) average temperature of measuring points and heat transfer wall temperature under different flow rates; (b) temperature distribution of heat transfer surface; (c) temperature distribution of heater section in back row thermometer position; (d) temperature distribution of heater section in front row thermometer position.

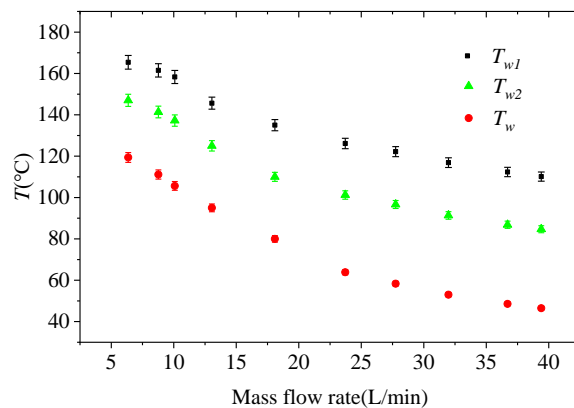


Figure 8. The relationship between the average wall temperature and the flow rate obtained.

The experimental data of single-phase water-cooled rectangular mini-channel with a large aspect ratio are provided and compared with Gnielinski [27], Forrest [14], and Dittus–Boelter heat transfer correlations. Gnielinski heat transfer correlations (28–29) are applicable to the turbulent transition region of $3000 < Re < 5 \times 10^6$.

$$Nu_f = \frac{\left(\frac{f}{2}\right)(Re_f - 1000)Pr_f}{1 + 12.7\left(\frac{f}{2}\right)^{\frac{1}{2}}\left(Pr_f^{\frac{2}{3}} - 1\right)} \quad (21)$$

$$f = \frac{1}{[3.64 \lg(Re) - 3.28]^2} \quad (22)$$

By modifying the formula in reference [27], Forrest obtained the following heat transfer correlation Equations (23) and (24), which are suitable for the heat transfer condition of one side heating and one side adiabatic in a rectangular small channel at high Re and with $Pr > 0.5$.

$$Nu_f = \frac{0.199(Re - 600)^{\frac{7}{8}}Pr}{5(Pr - 2)\phi^{\frac{1}{8}} + 10.05(Re - 600)^{\frac{1}{8}}\phi^{\frac{1}{4}}} \quad (23)$$

$$\phi^* = \frac{2}{3} \left(1 + \frac{W}{H}\right)^2 \times \left[1 - \frac{192W}{\pi^5 H} \sum_{n=0}^{\infty} \frac{1}{(2n+1)^5} \tanh\left\{\frac{(2n+1)\pi H}{2W}\right\}\right] \quad (24)$$

where ϕ^* is a geometric function, determined by W channel width and H channel height. The Dittus–Boelter heat transfer correlation in the turbulent region is as follows:

$$Nu_f = 0.023Re_f^{0.8}Pr_f^{0.4} \quad (25)$$

Figure 9 is the comparison between the correlation and the experimental data. It can be shown that the maximum deviation between Forrest correlation and the experimental data is less than 8% when $Re > 6000$, and the correlation between Dittus–Boelter and Gnielinski is more accurate to predict the experimental data when $Re < 6000$. Within the above Re range, the maximum deviations between Gnielinski and Dittus–Boelter formulas with experimental data are 10% and 12%, respectively. For the Dittus–Boelter formula, the large deviation at high Re may be the cause of uneven heating. According to the comparison with the correlations, it can be considered that the experimental data in this study are reliable. In the design of the split target, the heat transfer correlation can be used to predict the heat transfer effect inside the target. When Re reaches 21,000, Nu can reach 160.

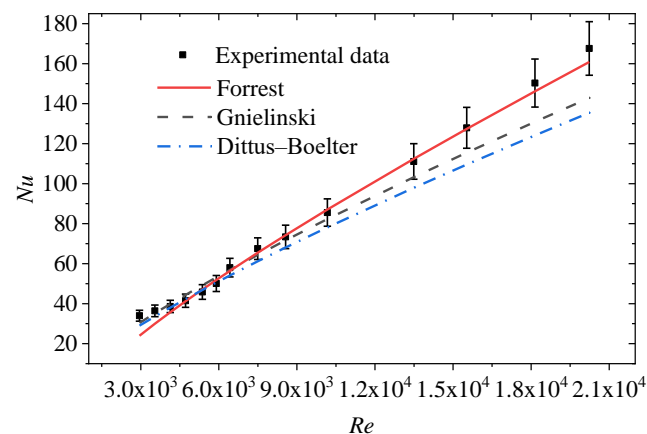


Figure 9. Heat transfer correlation with experimental data under constant Re .

4.2. Flow Characteristics Analysis

The friction pressure gradient along a channel may be expressed as follows:

$$-\left(\frac{dP}{dz}\right)_{friction} = \frac{1}{2}f \frac{\rho u_b^2}{D_{hyd}} \quad (26)$$

where f is the Darcy friction factor. In laminar flow, an exact solution for the velocity profile, and therefore the friction factor, is available for rectangular channels as follows:

$$f = \frac{64}{Re} \quad (27)$$

For turbulent flow, circular tube correlations are typically used with the hydraulic diameter in place of the tube diameter. Blasius [28] provided the following relation for the fully developed, turbulent friction factor in a smooth tube:

$$f = 0.3164Re^{-0.25} \quad (28)$$

Figure 10 shows the relationship between the drag coefficient and Re , with the increase of Re ; the drag coefficient decreases gradually. The correlations of laminar and turbulent flow (Blasius equation) calculated by $64/Re$ are used to predict for comparison. It can be concluded from the graph that when the Re reaches 2800, the resistance coefficient decreases sharply. According to the resistance coefficient value, it can be concluded that the critical Re of the rectangular channel under this size is between 2800 and 3800. The flow develops into complete turbulence when $Re > 6000$, which is consistent with the critical Re of the rectangular channel proposed by Bhatti and Shah [29]. In addition, the study in [29] points out that there are also signs of secondary flows in rectangular channels, although the size of these secondary flows may only be about 1/10 of the speed of primary flows. However, compared with the pipe with the same hydraulic diameter, the existence of secondary flow leads to the increase of frictional pressure drop, and the turbulent friction coefficient monotonically increases with the increase of the aspect ratio of the channel [30]. In the case of unilateral heating, the nonuniformity of fluid heating makes the prediction of rectangular channels more complicated.

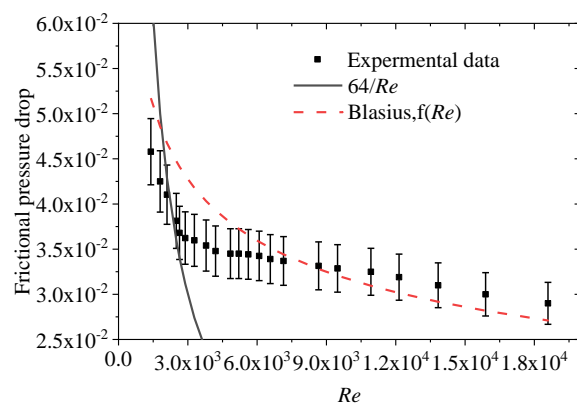


Figure 10. Drag coefficient with experimental data under constant Re .

4.3. Comparison of Experimental and Numerical Simulation

The experimental flow and heat transfer process was simulated by the CFD method. Figures 11 and 12 show a comparison of the simulation results with the experimental results. The maximum deviation of Nu and pressure drop are 8.2% and 11%, respectively, which indicates that the simulation results are in good agreement with the experimental data, demonstrating the feasibility of the numerical simulation approach. Furthermore, it is shown that the heat transfer effect is enhanced with the increase of Re . When the Re exceeds

6000, the turbulence develops into a complete turbulent state, which intensifies the flow heat transfer, thus leading to an increase in the proportion of the heat transfer coefficient.

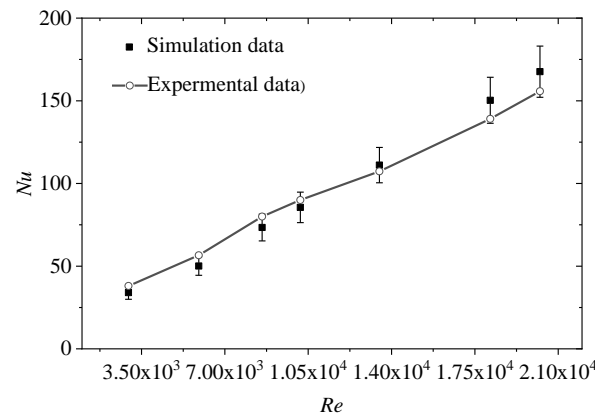


Figure 11. Validation of Nu for different Re .

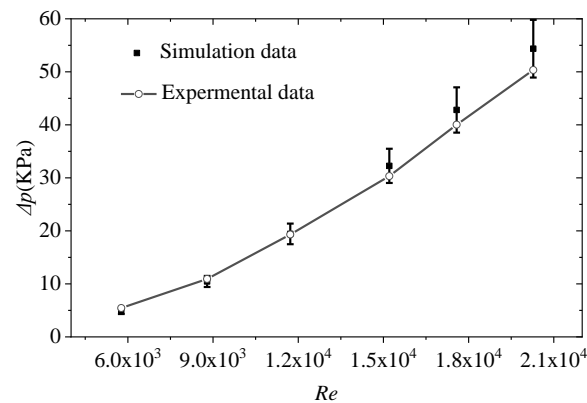


Figure 12. Validation of pressure drop for different Re .

4.4. Influence of Aspect Ratio on Flow Resistance

In the target design process, the channel thickness will affect the solid volume fraction of the target and ultimately affect the neutron production efficiency of the target. Therefore, it is necessary to explore the influence of width-to-height ratio on flow and heat transfer under the condition of height determination. From Equation (27), it is evident that in the heat transfer process of small channels, the heat transfer coefficient changes with Re and Pr , and the structural change has no effect on Nu . However, for the flow resistance, different structures will affect the flow resistance coefficient. In this study, the relationship between aspect ratio and pressure drop is studied by numerical method, and the simulation conditions are the same as Section 3.2. From Figure 13, it can be inferred that the logarithm of pressure drop shows a linear relationship with the logarithm of aspect ratio when the channel length is 170 mm and the height is 70 mm, and the pressure drop increases with the increase of aspect ratio and Re . The classical least squares method was used to evaluate the regression analysis coefficient. The relationship between the height–width ratio and pressure drop is defined in Equation (29). In this relationship, the height–width ratio is used as a reference parameter for dimensionless definition. The experimental results are in good agreement with the predicted data, and the maximum deviation of pressure drop is 10%.

$$\Delta P = 8.8 \times 10^{-9} \times Re^{1.8} \times \alpha^{2.9} \quad (29)$$

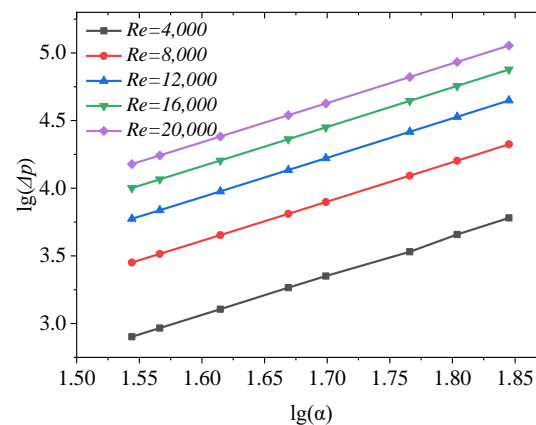


Figure 13. Logarithmic relationship between aspect ratio and pressure drop.

5. Conclusions

In this study, we introduced a mini-channel skin for cooling spallation target. An experimental study was performed to measure the single-phase friction factor and Nusselt number for a high aspect ratio, rectangular mini-channel heated on one side. The main findings can be summarized as follows:

1. The classical empirical formula of the circular tube cannot be used to predict the heat transfer coefficient of mini-channels with a large aspect ratio. After the characteristic length is corrected according to the aspect ratio, it can be predicted by the empirical formula of the rectangular channel. The simulation results of the K-Omega SST model are in good agreement with the experimental results, which verifies the correctness of the numerical method and can be used for target design.
2. The correlation between mini-channel pressure drop and aspect ratio was obtained, and the absolute error between the correlation and the experimental value was 6%.
3. The critical Re of the rectangular mini-channel is between 2800 and 3800.

Author Contributions: Conceptualization, T.L.; methodology, P.S.; software, P.S.; validation, Y.L. (Yiping Lu); formal analysis, L.Z.; investigation, J.T., P.S.; data curation, P.S.; writing—original draft preparation, P.S.; writing—review and editing, P.S.; visualization, Y.L. (Youlian Lu); supervision, J.T.; project administration, J.T.; funding acquisition, T.L. All authors have read and agreed to the published version of the manuscript.

Funding: This research was funded by the Program for Guangdong Introducing Innovative and Entrepreneurial Teams, grant number 2017ZT07S225 and the APC was funded by Guangdong Introducing Innovative and Entrepreneurial Teams.

Acknowledgments: This article Supported by the Program for Guangdong Introducing Innovative and Entrepreneurial Teams. (Project number: 2017ZT07S225).

Conflicts of Interest: The authors declare no conflict of interest.

Nomenclature

D_{hyd}	Hydraulic diameter, -
W	Width of the heating surface, m
S	Channel area, m^2
L	Length of the heating surface, m
H	Height of the heating surface, m
P	Wet perimeter, m
T_f'	Inlet temperature, K
T_f''	Outlet temperature, K
Q	Heating power, W

P	Density, Kg/m ³
C_p	Specific heat capacity, J/kg K ⁻¹
q_v	Volume flow, m ³ /s
h_{con}	Heat transfer coefficient, Wm ⁻² K ⁻¹
A_{con}	Heat exchange area, m ²
$\overline{T_w}$	Heat transfer surface average temperature, °C
$\overline{T_{w1}}$	Temperature of heater section in back row thermometer position, °C
$\overline{T_{w2}}$	Temperature of heater section in up row thermometer position, °C
Nu	Nusselt number, -
k	Fluid thermal conductivity, Wm ⁻¹ K ⁻¹
Re	Reynolds number, -
\bar{u}	Average axial velocity, m/s
Δp	Pressure drop, kpa
x	Thermometer distance, m
f	Resistance coefficient, -
U_{V_i}	Absolute uncertainty, -
V_i	Independent parameter, -
ϕ^*	Geometric function, -
Pr	Prandtl number, -
Γ_ω	Effective diffusion coefficient, -
Y_ω	Turbulent dissipation, -
k	Turbulent kinetic energy, J
ω	Specific dissipation rate, -
ν	Dynamic viscosity, pa/s
α	Aspect ratio, -

References

1. Wilcox, D.; Loveridge, P.; Davenne, T.; Jones, L.; Jenkins, D. Stress levels and failure modes of tantalum-clad tungsten targets at ISIS. *J. Nucl. Mater.* **2017**, *506*, 76–82. [\[CrossRef\]](#)
2. Naoe, T.; Futakawa, M. Pressure wave-induced cavitation erosion in narrow channel of stagnant mercury. *Trans. JSME* **2014**, *80*, fe0025-1-12. (In Japanese)
3. Riemer, B.; Wohlmuther, M.; Takada, H.; Takashi, N. Spallation Target Developments. In Proceedings of the ThEC13 Conference, Geneva, Switzerland, 27–31 October 2013; pp. 273–277.
4. Tuckerman, D.B.; Pease, R.F.W. High-performance heat sinking for VLSI. *IEEE Electr. Device Lett.* **1981**, *2*, 126–129. [\[CrossRef\]](#)
5. Murshed, S.; Nieto, C. A critical review of traditional and emerging techniques and fluids for electronics cooling. *Renew. Sustain. Energy Rev.* **2017**, *78*, 821–833. [\[CrossRef\]](#)
6. Kilic, M.; Aktas, M.; Sevilgen, G. Thermal Assessment of Laminar Flow Liquid Cooling Blocks for LED Circuit Boards Used in Automotive Headlight Assemblies. *Energies* **2020**, *13*, 1202. [\[CrossRef\]](#)
7. Liu, N.X.; Chen, H.; Wang, X.; Kefayati, G. Study on Surface Condensate Water Removal and Heat Transfer Performance of a Minichannel Heat Exchanger. *Energies* **2020**, *13*, 1065. [\[CrossRef\]](#)
8. Ghasemi, S.E.; Ranjbar, A.A.; Hosseini, M.J. Experimental and numerical investigation of circular minichannel heat sinks with various hydraulic diameter for electronic cooling application. *Microelectron. Reliab.* **2017**, *73*, 97–105. [\[CrossRef\]](#)
9. Yang, X.H.; Tan, S.C.; Ding, Y.J.; Liu, J. Flow and thermal modeling and optimization of micro/mini-channel heat sink. *Appl. Therm. Eng.* **2017**, *117*, 289–296. [\[CrossRef\]](#)
10. Muhammad, S.A.; Anwar, Z.; Mujtaba, M.A.; Soudagar, M.E.M.; Badruddin, I.A.; Safaei, M.R.; Iqbal, A.; Afzalqk, A.; Razzaqa, L.; Khidmatgar, A.; et al. Two-phase frictional pressure drop with pure refrigerants in vertical mini/micro-channels. *Case Stud. Therm. Eng.* **2021**, *23*, 100824.
11. Bagherzadeh, S.A.; Jalali, E.; Sarafraz, M.M.; Akbari, O.A.; Karimipour, A.; Goodarzi, M.; Bach, Q.V. Effects of magnetic field on micro cross jet injection of dispersed nanoparticles in a microchannel. *Int. J. Numer. Method Heat* **2020**, *30*, 2683–2704. [\[CrossRef\]](#)
12. Jasiński, P.B.; Kowalczyk, M.J.; Romaniak, A.; Warwas, B.; Obidowski, D.; Gutkowski, A. Investigation of Thermal-Flow Characteristics of Pipes with Helical Micro-Fins of Variable Height. *Energies* **2021**, *14*, 2048. [\[CrossRef\]](#)
13. Fialová, D.B.; Jegla, Z. Experimentally Verified Flow Distribution Model for a Composite Modelling System. *Energies* **2021**, *14*, 1778. [\[CrossRef\]](#)
14. Forrest, E.C.; Hu, L.W.; Buongiorno, J.; McKrell, T.J. Convective Heat Transfer in a High Aspect Ratio Mini-channel Heated on One Side. *J. Heat Transf.* **2015**, *138*, 021704. [\[CrossRef\]](#)
15. Wei, Z.Z.; Gao, L.S. Simulation and Experimental Research on Heat Transfer of Metal Microchannel Heat-sink. *Vac. Cryog.* **2020**, *26*, 131–138.
16. Muhammad, A.; Selvakumar, D.; Wu, J. Numerical investigation of laminar flow and heat transfer in a liquid metal cooled mini-channel heat sink. *Int. J. Heat Mass Transf.* **2020**, *150*, 119265. [\[CrossRef\]](#)

17. Ahmadi, A.A.; Arabbeiki, M.; Muhammad A., H.; Goodarzi, M.; Safaei, M.R. Configuration and Optimization of a Minichannel Using Water-Alumina Nanofluid by Non-Dominated Sorting Genetic Algorithm and Response Surface Method. *Nanomaterials* **2020**, *10*, 901. [[CrossRef](#)]
18. Hassan, M.; Sadri, R.; Ahmadi, G.; Dahari, M.B.; Kazi, S.N.; Safaei, M.R.; Sadeghinezhad, E. Numerical Study of Entropy Generation in a Flowing Nanofluid Used in Micro- and Minichannels. *Entropy* **2013**, *15*, 144–155. [[CrossRef](#)]
19. Zheng, W.; Sun, J.J.; Ma, C.B.; Yu, Q.P.; Zhang, Y.N.; Niu, T. Numerical Study of Fluid Flow and Heat Transfer Characteristics in a Cone-Column Combined Heat Sink. *Energies* **2021**, *14*, 1605. [[CrossRef](#)]
20. Worwood, D.; Marco, J.; Kellner, Q.; Hosseinzadeh, E.; McGlen, R.; Mullen, D.; Lynn, K.; Greenwood, D. Experimental Analysis of a Novel Cooling Material for Large Format Automotive Lithium-Ion Cells. *Energies* **2019**, *12*, 1251. [[CrossRef](#)]
21. Allio, A.; Difonzo, R.; Leggieri, A.; Legrand, F.; Marchesin, R.; Savoldi, L. Test and Modeling of the Hydraulic Performance of High-Efficiency Cooling Configurations for Gyrotron Resonance Cavities. *Energies* **2020**, *13*, 1163. [[CrossRef](#)]
22. Li, S.L.; Zhao, Z.C.; Zhang, Y.Z.; Xu, H.J.; Zeng, W.Q. Experimental and Numerical Analysis of Condensation Heat Transfer and Pressure Drop of Refrigerant R22 in Minichannels of a Printed Circuit Heat Exchanger. *Energies* **2020**, *13*, 6589. [[CrossRef](#)]
23. Moody, L. Friction Factors for Pipe Flow. *Trans. ASME* **1944**, *66*, 671–684.
24. Incropera, F.P.; Dewitt, D.P.; Bergman, T.L.; Lavine, A.S. *Fundamentals of Heat Mass Transfer*; John-Wiley Sons: New York, NY, USA, 1996.
25. Schultz., R.; Cole, R. Uncertainty analysis in boiling nucleation. *Aiche Symp. Ser.* **1979**, 7532–7538.
26. Roache, P.J. Perspective: A method for uniform reporting of grid refinement studies. *J. Fluids Eng.* **1994**, *116*, 405–413. [[CrossRef](#)]
27. Gnielinski, V. New equations for heat and mass transfer in turbulent pipe and channels flow. *Int. Chem. Eng.* **1976**, *16*, 359–368.
28. Shah, R.K. Laminar flow friction and forced convection heat transfer in ducts of arbitrary geometry. *Int. J. Heat Mass Transf.* **1975**, *18*, 849–862. [[CrossRef](#)]
29. Bhatti, M.S.; Shah, R.K. Turbulent and Transition Flow Convective Heat Transfer in Ducts. In *Handbook of Single-Phase Convective Heat Transfer*; John-Wiley Sons: New York, NY, USA, 1987.
30. Jones, O.C. An improvement in the calculation of turbulent friction in rectangular ducts. *J. Fluid Eng. ASME* **1976**, *98*, 173–180. [[CrossRef](#)]